Chemical Science

ROYAL SOCIETY OF CHEMISTRY

EDGE ARTICLE

View Article Online
View Journal | View Issue

Cite this: *Chem. Sci.*, 2024, **15**, 6906

All publication charges for this article have been paid for by the Royal Society of Chemistry

Received 2nd January 2024
Accepted 31st March 2024

DOI: 10.1039/d4sc00009a

rsc.li/chemical-science

Robust vibrational coherence protected by a core–shell structure in silver nanoclusters†

Jie Kong, ‡[a] Zhuoran Kuang, ‡[b] Wei Zhang, ‡[a] Yongbo Song, *[c] Guo Yao,[d] Chunfeng Zhang,[d] He Wang,[e] Yi Luo *[a] and Meng Zhou *[a]

Vibrational coherence has attracted considerable research interests because of its potential functions in light harvesting systems. Although positive signs of vibrational coherence in metal nanoclusters have been observed, the underlying mechanism remains to be verified. Here, we demonstrate that robust vibrational coherence with a lifetime of 1 ps can be clearly identified in $Ag_{44}(SR)_{30}$ core–shell nanoclusters, in which an icosahedral Ag_{12} core is well protected by a dodecahedral Ag_{20} cage. Ultrafast spectroscopy reveals that two vibrational modes at around 2.4 THz and 1.6 THz, corresponding to the breathing mode and quadrupolar-like mode of the icosahedral Ag_{12} core, respectively, are responsible for the generation of vibrational coherence. In addition, the vibrational coherence of Ag_{44} has an additional high frequency mode (2.4 THz) when compared with that of Ag_{29}, in which there is only one low frequency vibration mode (1.6 THz), and the relatively faster dephasing in two-layer Ag_{29} relative to that in Ag_{44} further supports the fact that the robust vibrational coherence in Ag_{44} is ascribed to its unique matryoshka-like core–shell structure. Our findings not only present unambiguous experimental evidence for a multi-layer core–shell structure protected vibrational coherence under ambient conditions but also offers a practical strategy for the design of highly efficient quantum optoelectronic devices.

Introduction

Coherence refers to the oscillatory behavior that is the superposition on the excited state, which is widely observed in many different systems, such as isolated molecules, semiconductors, as well as metal nanoparticles (NPs).[1–7] For isolated molecules, coherences arise from the wave packet moving on the potential energy surface of the excited- or ground-state which leads to the enhancement or depletion in intensity.[8–11] It was also observed that the vibrational coherence can transfer from one excited state potential energy surface to another, and this can be used to drive the intersystem crossing (singlet–triplet conversion) process, track the electron transfer, and analyze the structural variables,[12–16] while the coherent oscillations of the metal NPs are due to the lattice expansions from the laser heating effect, which can be modulated by the size and shape.[6,17] Metal nanoclusters (NCs) are sub-2 nm nanoparticles that possess a discrete energy level because of the quantum confinement effect.[18–20] Because coherence is an important property in other systems, and widely applied, the coherence of the metal NCs that are newly observed using broadband transient absorption (TA) spectroscopy have attracted great attention in recent years.[21–33]

It is known that in organic molecules, the soft structure can accelerate the dephasing of the coherence because of the fast energy transfer to the environment, whereas in solid-state systems including inorganic semiconductors and metals, phonons and surface defects can cause significant decoherence.[1] Conversely, the vibrational coherence can be easily perturbed by the solvent fluctuation and environmental heat, which will significantly accelerate the damping of the coherent oscillations.[22] In this context, metal NCs have attracted considerable research interest, and they can serve as an intermediate state between metallic nanoparticles and isolated metal atoms.[34–36] For instance, gold and silver NCs exhibit discrete energy levels and multiple absorption bands that arise from single exciton transitions, making them potential

[a]*Hefei National Research Center for Physical Sciences at the Microscale, University of Science and Technology of China, Hefei, Anhui 230026, P. R. China. E-mail: yiluo@ustc.edu.cn; mzhou88@ustc.edu.cn*

[b]*State Key Laboratory of Information Photonic and Optical Communications, School of Science Beijing University of Posts and Telecommunications (BUPT), Beijing 100876, P. R. China*

[c]*School of Biomedical Engineering, Research and Engineering Center of Biomedical Materials, Anhui Medical University, Hefei, Anhui 230032, P. R. China. E-mail: ybsong860@ahmu.edu.cn*

[d]*National Laboratory of Solid State Microstructures, School of Physics, Collaborative Innovation Center for 5Advanced Microstructures, Nanjing University, Nanjing 210093, P. R. China*

[e]*Department of Physics, University of Miami, Coral Gables, Florida 33146, USA*

† Electronic supplementary information (ESI) available. See DOI: https://doi.org/10.1039/d4sc00009a

‡ These authors contributed equally.

candidates for light harvesting nanomaterials.[37–39] Ligand-protected metal NCs show well-defined structures, and it is possible to correlate the optical properties with their atomic structures.[37] Many of these thiolate-protected gold and silver NCs are made of a metal core protected by a shell structure that consists of metal atoms, such as surface sulfur atoms and carbon tails.[36,37,40] Using an ultrafast laser to selectively excite the vibrations of the metal core, signs of vibrational coherence have been observed in the excited state dynamics of metal NCs.[25,26,41,42] However, the underlying mechanism needs to be further verified as coherent vibrational modes involved are difficult to identify, and the fast decoherence has complicated the entire analysis. A previous study assigned coherent vibrations in several gold NCs to mechanical vibrations similar to those in large metallic gold nanoparticles, which are typically induced by ultrafast laser heating.[24] Further experimental research and theoretical work are needed to assign the vibration modes and design metal NCs with slow decoherence.

Here, we chose $[Ag_{44}(SR)_{30}]^{4-}$ (SR = $SPhF_2$, Ag_{44} for short) as a model system to understand the vibrational coherence in silver NCs. Femtosecond transient absorption measurements indicate that the excited state absorption and ground state bleaching of Ag_{44} exhibit mirror-image dynamics, suggesting similar excited state and ground state electronic structures. Significant vibrational coherences with frequencies around 2.4 THz and 1.6 THz can be observed in TA spectra, and the decay time of the coherent oscillations is around 1 ps. Theoretical calculation results indicate that these two modes arise from the breathing and quadra-polar like modes of the metal core in Ag_{44}, respectively. The analysis of the damping of the coherent oscillations indicates that the robust coherence is protected by the three-layer core–shell structure in Ag_{44} during the excited state relaxation.

Results and discussion

The structure of the Ag_{44} NCs consists of an Ag_{32} core, which can be described as a three layer matryoshka-like core–shell structure (Fig. 1A).[36] The first layer is a hollow icosahedral cage of Ag_{12}, and the second layer is a dodecahedral Ag_{20} cage. The two-layer Ag_{32} core is protected by six $Au_2(SR)_5$ motifs (third layer) to form the $Ag_{44}(SR)_{30}$ structure. To characterize electron-vibration interactions in the Ag_{44} NCs, we first measured the temperature-dependent electronic absorption spectrum. As shown in Fig. 1B, six excitonic peaks dominated the electronic absorption spectrum between 300 nm and 1100 nm at room temperature (295 K), which agrees with those found in a previous work.[36] Upon decreasing the temperature from 295 K to 78 K, it was observed that: (1) all those six absorption peaks become sharper and stronger; (2) the positions of five absorption peaks between 300 nm and 800 nm are apparently blue shifted (Fig. S1†), whereas the position of the absorption band at around 850 nm remains unchanged (Fig. 1B). A similar trend in the absorption spectra at cryogenic temperatures has been reported for several Au nanoclusters, which was explained as electron-vibration coupling within the metal core and on surface motifs.[43,44] The strong temperature dependence of the electronic absorption spectrum suggests that significant electron-vibrational coupling occurs in Ag_{44}. Further, the temperature dependent full width at half maximum (FWHM) at ~610 nm was extracted and is presented in Fig. S2,†[45–49] which gives a strength of $\gamma_{LO} = 17$ meV for the coupling between an optical phonon with an electron.

Unlike $[Au_{25}(SR)_{18}]^-$ (Au_{25} for short) which shows splitting in the lowest absorption band at cryogenic temperatures,[43,44] the lowest energy absorption band in Ag_{44} remains as a single peak at 78 K. Previous theoretical calculations on Ag_{44} reported that the lowest energy absorption band around 1.5 eV arose from HOMO to LUMO+1, whereas the HOMO → LUMO transition is dipole-forbidden.[36] The optical energy gap at room temperature estimated from the absorption spectrum is around 1.2 eV (see Fig. S1†), and the photoluminescence was reported to be centered around 1400 nm (0.88 eV),[50] which gives a large Stokes shift of 0.32 eV.

To understand the nature of the transition of the lowest-energy absorption band and property of the excited state, quantum chemical calculations were performed using density functional theory (DFT) and time-dependent density functional theory (TDDFT) methods.[51,52] Before calculating the electronic transition, the structure was completely relaxed. Fig. S3† displays the isosurface of frontier orbitals of the Ag_{44} nanocluster. The HOMO and HOMO-1 of Ag_{44} show a delocalized distribution on the second shell of the cluster (Ag_{20} cage). The LUMO+1 is symmetrically distributed on the four vertices of the Ag_{20} cage, whereas the LUMO is concentrated on the Ag_{12} core (see Fig. 1C). It was found that $S_0 \rightarrow S_1$ is mainly contributed by the HOMO to LUMO transition (98%), and the oscillator strength is very weak ($f = 0$). $S_0 \rightarrow S_2$ comes from the HOMO-1 to LUMO transition (98%) with an oscillator strength of 0, and $S_0 \rightarrow S_3$ which stems from the HOMO to LUMO+1 transition with an oscillator strength of $f = 0.0054$ (see Table S1†). The results indicate that the HOMO → LUMO transition is dipole-forbidden, and the lowest-energy optical transition is HOMO → LUMO+1, which agrees with the previous work on all-thiol-stabilized Ag_{44}.[21]

The analysis of hole–electron distributions is performed to reveal the features of S_{1-3} states.[53] The charge density differences (CDDs) between S_1/S_3 and S_0 states at optimized S_0 geometries of Ag_{44} were calculated by using $\Delta\rho(r) = \rho^{ele}(r) - \rho^{hole}(r)$, and obtained CDDs are displayed in Fig. S4.† The TDDFT calculation results display the charge transefer (CT) feature in the $S_0 \rightarrow S_3$ transition, the CT excited state further deactivation to fully charge transfer ($Ag_{20} \rightarrow Ag_{12}$, CS) state ($S_1$), and then charge recombination. The photoluminescence was previously reported to be 1400 nm (0.88 eV),[50] which is consistent with the energy of the CS state (0.899 eV) as shown in Table S1†.

Before examining the coherence dynamics of Ag_{44}, we first used femto-nanosecond transient absorption (TA) spectroscopy to analyze the population dynamics. We chose to pump at 400 nm (3.1 eV) and 900 nm (1.38 eV) to selectively excite the NCs to higher and lower excited states to obtain complete relaxation dynamics. In the TA spectra of Ag_{44}, excited state absorption (ESA, positive signal) and ground state bleaching (GSB, negative signal) are sharp and less overlapped (Fig. 2A, B

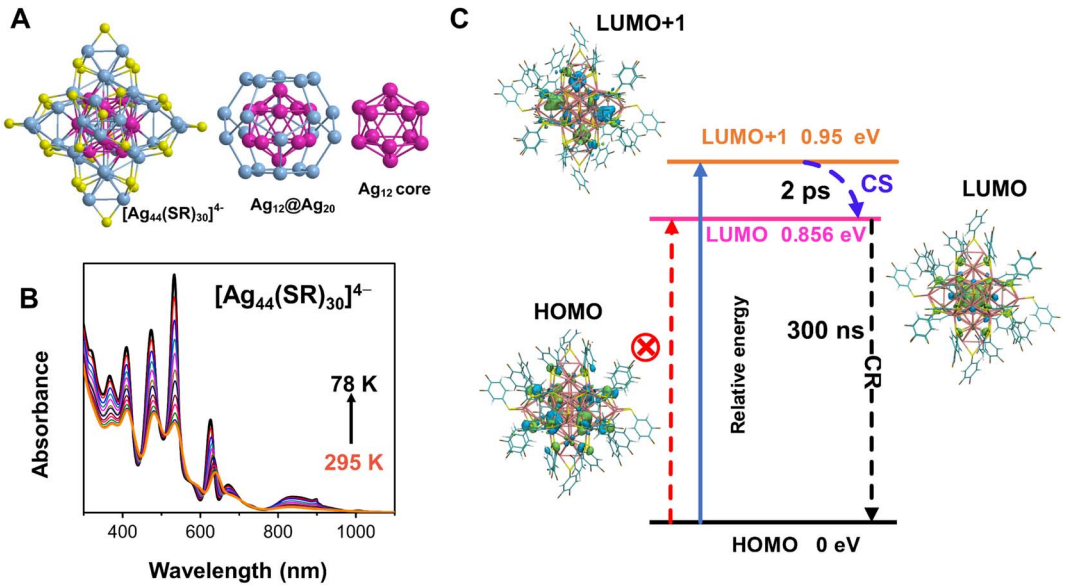

Fig. 1 (A) Crystal structure of $[Ag_{44}(SR)_{30}]^{4-}$, the icosahedral Ag_{12} core (carmine), and the dodecahedral Ag_{20} cage (light blue); (B) steady state electronic absorption spectra of Ag_{44} NCs in 2-methyltetrahydrofuran as a function of temperature at the wavelength scale; (C) molecular orbital distributions and relaxation pathways obtained from DFT calculations. The time constants were obtained from the time-resolved transient absorption data. CS: charge separation; CR: charge recombination.

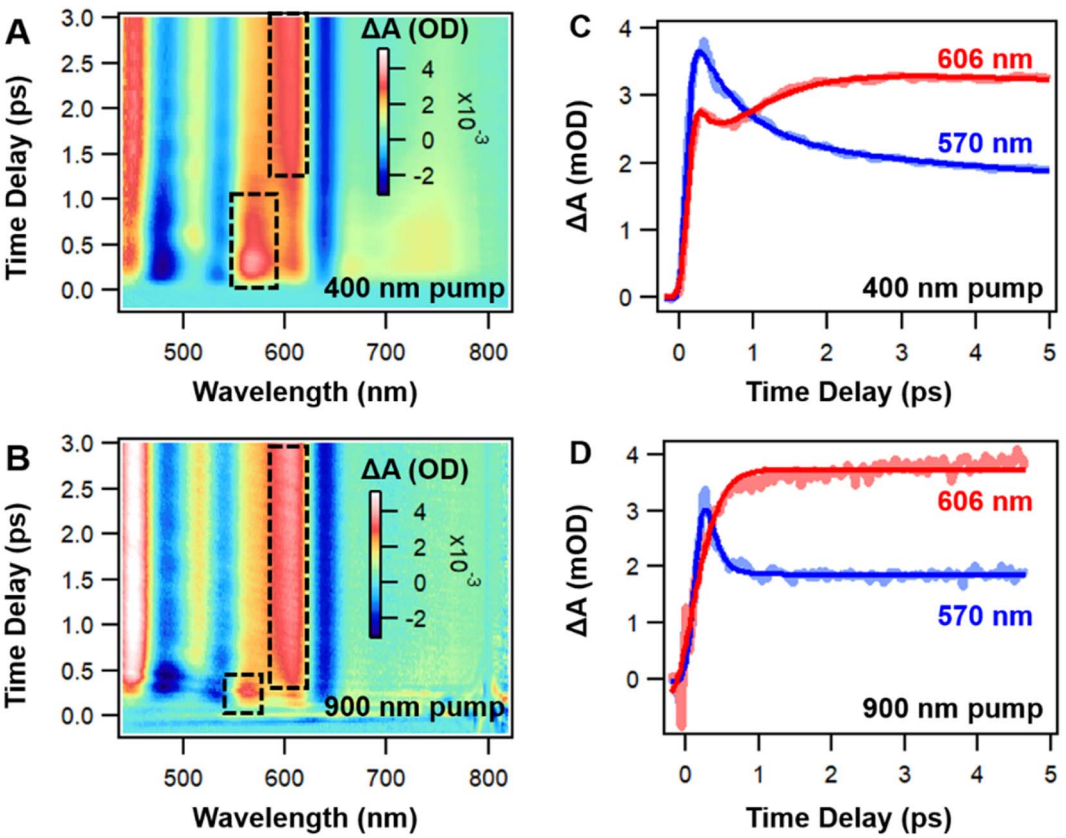

Fig. 2 (A) The TA data map with 400 nm excitation between −0.2 and 3 ps; (B) the TA data map with 900 nm excitation between −0.2 and 3 ps; (C) TA kinetic traces and fitting with 400 nm excitation; (D) TA kinetic traces and fitting with 900 nm excitation.

and S5†). In the initial 3 ps, with 400 nm and 900 nm excitations, significant spectral evolution was observed between 550 nm and 620 nm. The ESA probe at 570 nm decays, and the ESA probe at 606 nm increases at the same time (Fig. 2C and D), which indicates a two-state relaxation model. It should be noted that relative to the excitation under 900 nm, there is an additional ESA band located at the 680–720 nm (Fig. 1A) under 400 nm during the initial delay time, which is ascribed to high-energy populated excited states. The decay of this ESA can be ascribed to the internal conversion (IC) from a higher excited state to a lower excited state. Meanwhile, the excited state dynamics of Ag_{44} are totally independent of pump fluences (Fig. S6†), ruling out auger recombination as a possible relaxation pathway. From 10 ps to 10 ns, the TA spectra remains unchanged, and there is no spectral evolution (Fig. S5†), and the lifetime of the final excited state is around 300 ns. In a previous work, a long-lived charge separation state has been proposed as the final excited state of the Ag_{44} NCs.[54] Considering the large Stokes shift and two-state relaxation process under both excitation conditions, our results indicate that the final long-lived state at around 0.88 eV should be a CS state, which agrees with DFT calculation results in Fig. 1C.

Because ESA and GSB peaks in Ag_{44} are well separated, it allows us to analyze the electron and hole dynamics, respectively. As shown in Fig. 3A, the GSB peaks around 480, 535 and 640 nm are marked as B3, B2 and B1, respectively, whereas the ESA peaks around 570, 603 and 780 nm are marked as A3, A1 and A2, respectively, (Fig. 3A). It is interesting to see that these three pairs of ESA and GSB peaks show mirror image dynamics, that is, A1 and B1, A2 and B2, A3 and B3 exhibit similar dynamics, respectively, (Fig. 3B). For the three GSB peaks, B3 decays to give rise to B2, and B2 decays give rise to B1. Similarly, A3 decays give rise to A2, and A2 decays to give rise to A1.

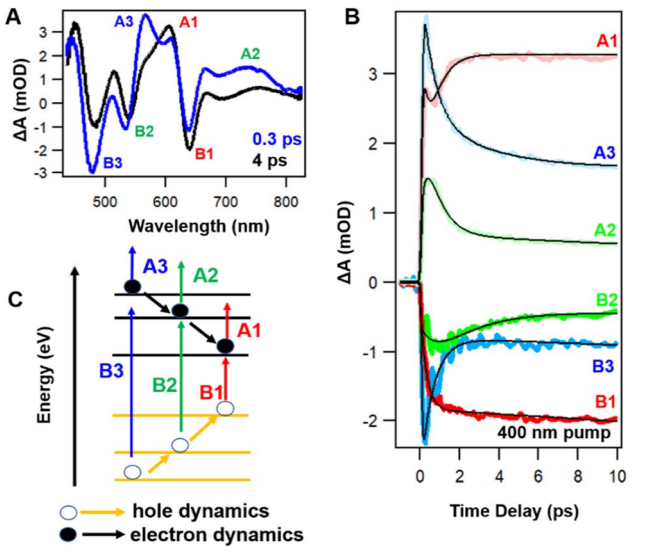

Fig. 3 Excited-state dynamics of Ag_{44} obtained from TA spectroscopy pumped at 400 nm. (A) The TA spectrum probed at 4 ps; (B) TA kinetic traces probed at selected wavelengths and their corresponding fitting; (C) energy diagram that describes the electron and hole dynamics of the Ag_{44} NCs.

All these ESA and GSB decays can be well fitted by a two-step sequential model (see Fig. S7†). Based on the data analysis, the relaxation pathway of Ag_{44} pumped at 400 nm is summarized in Fig. 3C. The relaxation of electrons and holes involve three steps: (1) a fast decay from a higher excited state to a lower excited state (IC process) in 0.5 ps, (2) a slow decay from a lower excited state to a charge separated state in 2 ps, and (3) a slow charge recombination from the CS state to the ground state in 300 ns. With 900 nm excitation, the mirror image dynamics of ESA and GSB still persist, and the relaxation only involves two steps: fast relaxation to a charge-separated state in 0.2 ps (see Fig. S8†) and the recombination of the CS state in 300 ns. The mirror image dynamics of ESA and GSB indicate that the excited states and ground states of Ag_{44} share very similar electronic structures. Such an observation could be explained by the highly symmetrical structure in the metal core of the Ag_{44} NCs.

In the initial 5 ps, significant ripples can be observed from the TA data map at almost all of the probe wavelengths under 400 nm and 900 nm excitations (Fig. 4A and S9A†), which indicated significant vibrational coherence. To obtain a clear picture of the coherence signal, we performed global fitting on the TA data of the Ag_{44} NCs to remove the population dynamics. The residual data as a function of time delay and probe wavelengths represent the distribution of the coherent oscillations (Fig. 4B and S9B†), which indicates wave packet motions. From the residual data map with 400 nm excitation, it was observed that: (1) oscillations probed between 420 nm and 620 nm showed slower damping, whereas those probed between 620 nm and 820 nm were damped more rapidly (see Fig. 4B); (2) the phase flip (node) can be observed around the ESA maximum of around 520 nm (Fig. 4B and D). Because the phase shift and amplitude node were observed in the residual data map, the coherence oscillations in Ag_{44} should arise from the modulation of the excited state absorption frequency.

Based on oscillation behaviors, we can divide the probe wavelength of the TA spectra into three regions: 480–520 nm, 525–580 nm, and 680–720 nm. The residual kinetics (oscillations) probed in each region are very similar so that we can average the TA kinetics in each region (Fig. 4C). We fit the residual kinetics in these three regions using a damped cosinusoidal function (see eqn S2–S6, ESI†) and obtained the phase and damping information of the oscillations (see Fig. 4C and S10†). The residual kinetics probed over the entire wavelength range exhibited two major vibration modes with periods of ~0.4 ps and ~0.6 ps. Moreover, the coherent oscillations probed between 680–720 nm had a damping time of ~0.25–0.5 ps, two–four times faster than the damping times of those probed in the other two regions (1.0 ps). Fig. S9C, D and Table S2† show the fitting results of the oscillations with 900 nm excitation. The periods and damping times of the oscillations are similar with those obtained with 400 nm excitation (Table 1).

The dephasing of vibrational coherence indicates the disappearance of the coherence between two states, while the disappearance of the oscillation can be ascribed to the depopulation of the excited state. The damping of the oscillations measures the decay time of the vibrations in the Ag_{44} NCs. The decay of the oscillations may arise from pure dephasing or

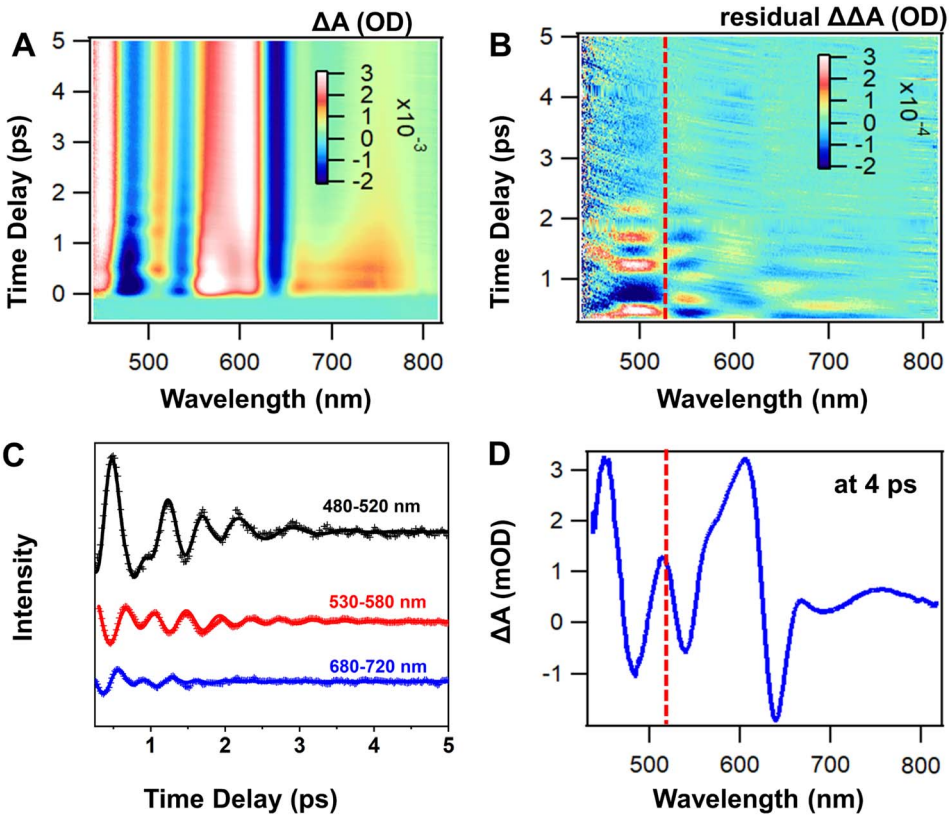

Fig. 4 (A) The TA data map of the Ag_{44} NCs pumped at 400 nm between −0.5 and 5 ps; (B) the TA data map after subtracting the population kinetics obtained from the global fitting, and red dashed lines indicate probe wavelengths where the phase shift occurs; (C) TA residuals as a function of the time delay of the Ag_{44} NC probe at selected wavelength regions and corresponding fits; (D) the TA spectrum of Ag_{44} probed at 4 ps, and the red dashed line indicates the probe wavelength where the phase shift occurs.

Table 1 Coherent oscillation results obtained from the fitting results of residual data of Ag_{44} with 400 nm excitation

Probe range (nm)	Period (ps)	Frequency (THz)	t_{damp} (ps)
480–520	0.41	2.43	1.04
	0.60	1.66	1.06
525–580	0.41	2.43	1.02
	0.61	1.64	1.04
680–750	0.37	2.69	0.23
	0.61	1.63	0.58

population relaxation.[55] With 400 nm excitation, the fast damping (0.25–0.5 ps) of the oscillations probed between 680 nm and 720 nm is consistent with the fast decay of the ESA band probed at the same region (see Fig. 3). In addition, it could be observed that no oscillations in 680–720 nm as well as in the IC process were obtained under 900 nm excitation. Therefore, the rapid disappearance of the oscillations with 400 nm excitation in this region should be related to the fast depopulation relative to other spectral region, and when the populations evolve from a higher to a lower excited state, the wave packet motion of the higher excited state should disappear quickly. This also explains the disappearance of the oscillations probed between 620 nm and 820 nm with 900 nm excitation, because the ESA band in this region remains unchanged during the probing time window. The relatively long-lived vibrational coherence (>1 ps) in Ag_{44} probed at other wavelengths indicated that the damping should arise from the pure dephasing from the energy disorder or fluctuations.[55]

The phase of the oscillations provides information on the starting time of the coherence.[8] According to a previous study of the coherence of organic molecules, the position of the phase flip can help identify the origin of the wave packet motions.[56] The phase flip at the GSB maximum indicates a ground state coherence, while the phase flip occurring at the maximum of the ESA or the stimulated emission (SE) indicates an excited state coherence.[8,57] Here, phase shift and zero amplitude are located at around 520 nm (Fig. 4B and D), which is around the ESA peak position. Therefore, excited state coherence is more likely to be responsible for these coherent oscillations.

To further obtain the frequency and amplitude distribution of the coherence, we performed fast Fourier transform (FFT) on the oscillations of each probe wavelength (residual data map) and from this obtained the FFT data map of Ag_{44} at 400 nm and 900 nm excitations (Fig. 5A and B). Two vibration modes with frequencies of 1.6 THz and 2.4 THz can be identified from the FFT data map, which agrees with the frequency obtained from the fitting results of the oscillations (Table 1). It is worth noting

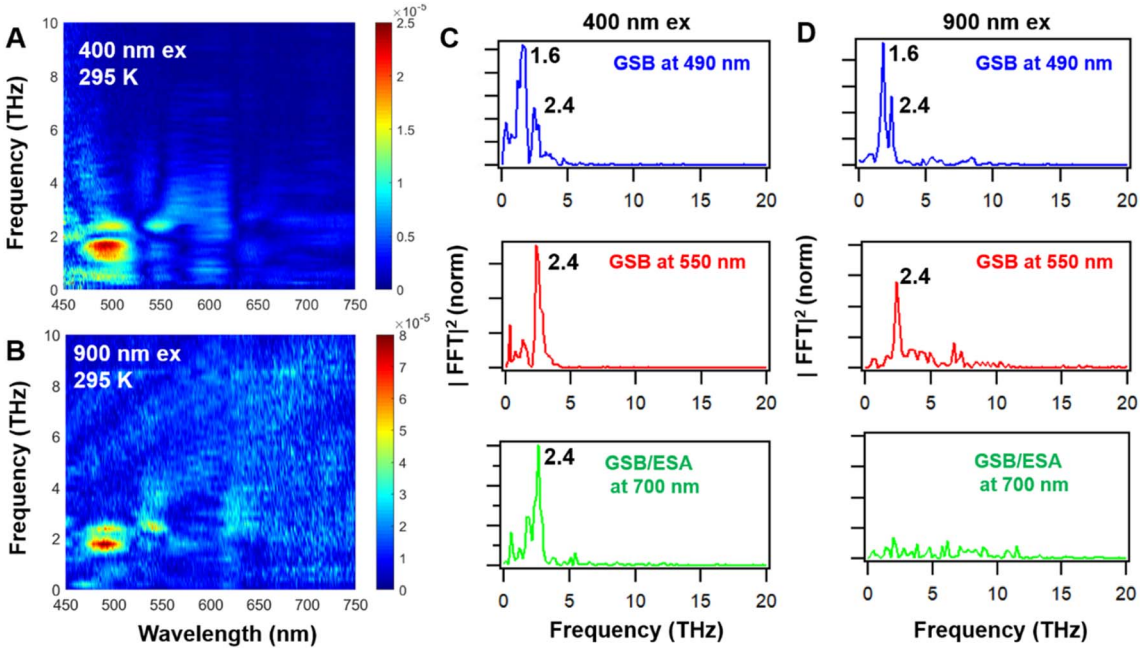

Fig. 5 FFT maps of wave packet-modulated TA spectra of Ag_{44} with excitation of (A) 400 nm and (B) 900 nm at room temperature. The FFT amplitude distribution at selected probe wavelengths with excitation of (C) 400 nm and (D) 900 nm.

that the 2.4 THz mode agrees with the results in a previous work on Ag_{44} NCs.[38]

From the FFT amplitude distribution (Fig. 5C and D) under both excitation conditions, it was found that 1.6 THz and 2.4 THz modes can be observed in the GSB and ESA between 470 nm and 520 nm, while the GSB peak at around 550 nm mainly shows the 2.4 THz mode. With the 900 nm excitation, the 2.4 THz mode disappears together with the ESA band at 700 nm, which agrees with the results in Fig. 3 and S7.† The observation of the two modes with 400 nm and 900 nm excitation indicates that the vibrational coherence in Ag_{44} (probed between 480 nm and 580 nm) can be generated regardless of the initial state prepared by the pump laser.

To reveal the nature of the low frequency vibration bands associated with Ag_{44}, theoretical computations of Raman spectra were performed. The calculated Raman spectrum (see Fig. S11†) shows three distinct and strong bands (1.8, 2.7 and 3.9 THz, *i.e.* 61.7, 92.7 and 130.0 cm^{-1}) in the low frequency region (<4.5 THz, 150 cm^{-1}) that are associated with the vibrations involving the Ag metal atom of the cores. These results are in good agreement with the experimental Raman spectrum (1.6, 3.0, 4.0 THz, *i.e.* 53, 103, 133 cm^{-1}) of Ag_{44} reported previously.[58] In the metal NCs, those vibrations with a frequency below 3 THz (100 cm^{-1}) were previously assigned to the acoustic vibration of the metal core. In $Au_{25}(SR)_{18}$ and $Au_{144}(SR)_{60}$ NCs, two vibration modes (2.4 THz and 1.2 THz for Au_{25} and 2 THz and 1.5 THz for Au_{144}) have been reported, and they were assigned to the breathing mode and quadrupolar-like mode that was dominated by icosahedral cores in Au_{25} and Au_{144}, respectively.[22,24,59] Similarly, the 2.4 THz mode observed in Ag_{44} should be assigned to the breathing vibration mode of the icosahedral Ag_{12} core, while the 1.6 THz mode should be assigned to the quadrupolar-like mode of icosahedral Ag_{12}. These two modes agree with the calculation results of the Raman modes of the Ag_{12} kernel (see Fig. S11 and 12†) at around 2.7 THz (61.7 cm^{-1}) and 1.8 THz (92.7 cm^{-1}).

To further understand the structural effect of the vibrational coherence in metal NCs, we chose $Ag_{29}BDT_{12}TPP_4$ (BDT: 1,3-benzenedithiol; TPP: triphenylphosphine) (Ag_{29} for short) NCs[60] and compared its vibrational coherence with that of Ag_{44}. Ag_{29} contains an icosahedral Ag_{13} core protected by a one layer silver shell (Fig. 6A), and it is an ideal model to probe the effect of surface layers on the vibrational coherence. Fig. 6B and C show the TA data map and fitting residual map of Ag_{29} with photoexcitation of 400 nm. Significant coherent oscillations can also be observed in the TA kinetics in the first 5 ps probed between 450 and 650 nm. The FFT data map of TA residuals shows a significant peak at around 1.6 THz (Fig. 6D, S13 and S14†), which is comparable to the quadrupolar-like mode (see Fig. 5) of icosahedral Ag_{12} in Ag_{44}. Therefore, in Ag_{44} and Ag_{29}, we observed the 1.6 THz mode from the icosahedral silver core. After fitting the TA residual kinetics, we found that the dephasing time of the vibrational coherence in Ag_{29} is shorter when compared to that of Ag_{44} (see Fig. 6E and S13†). The absence of the 2.4 THz mode in the Ag_{29} NCs should indicate an even faster decoherence, which is not resolved in our experiments. The fitting parameters of the oscillations of Ag_{29} are shown in Table 2. The relatively faster dephasing of vibrational coherence and fewer vibration modes in the two-layer Ag_{29} further supports the fact that the multi-layer core–shell structure can protect the vibrational coherence in the metal NCs. We further analysed the GSB position (~540 nm) of Ag_{44} at different time delays, and it was observed that the peak position shows a periodic shift with a period of ~0.4 ps (Fig.-S16A†), corresponding to frequency modulated oscillations

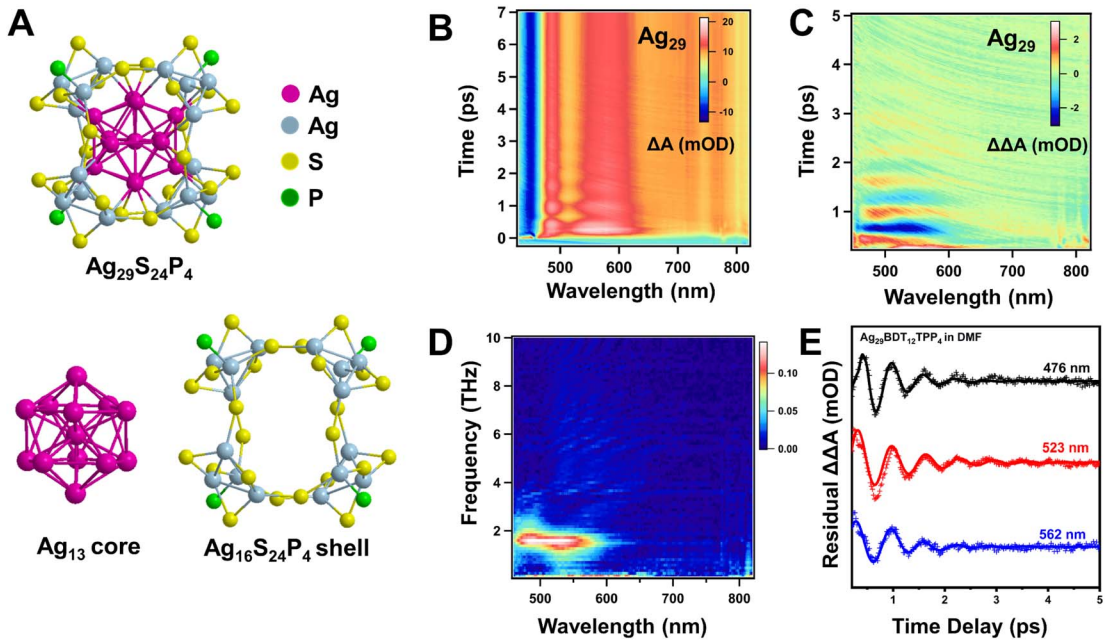

Fig. 6 (A) Crystal structure of $Ag_{29}S_{24}P_4$, the icosahedral Ag_{13} core (carmine), and the $Ag_{16}S_{24}P_4$ shell; (B) transient absorption data map of Ag_{29} with 400 nm excitation at 295 K; (C) the TA data map after subtracting the population kinetics obtained using global fitting; (D) FFT maps of the TA residual data of Ag_{29}; (E) TA residuals as a function of time delay of the Ag_{29} NC probe at selected wavelengths and corresponding fits.

Table 2 Coherent oscillation results obtained from the fitting results of the residual data of Ag_{29} with 400 nm excitation

Probe range (nm)	Period (ps)	Frequency (THz)	t_{damp} (ps)
476	0.61	1.64	0.53
523	0.63	1.59	0.91
562	0.64	1.57	0.51

(Fig. S16B†).[7] However, the TA spectral peak positions of Ag_{29} almost remained the same during the oscillation, and only the peak intensity shows a periodic change (Fig. S16C†), thus it can be assigned to amplitude modulated oscillations (Fig. S16D†).[7]

In a previous work on metal NCs, the strong vibrational coherence arises from the low frequency vibration of the inner metal core layer, while the role of the surface layers has not been well understood. It was also reported that icosahedral $[Au_{13}(dppe)_5Cl_2]^{3+}$ [dppe: 1,2-bis(diphenylphosphino)ethane)] NCs, with no core–shell structure, did not show significant coherent vibrations in time-resolved experiments.[42] However, strong coherent vibrations can be observed in $[Au_{25}(SR)_{18}]^-$ NC which contains an icosahedral Au_{13} core and a one layer shell consisting of four $Au_3(SR)_4$ motifs.[59] Recently, significant coherent vibrations were reported in $Au_{144}(SR)_{60}$ (ref. 61) (Au_{144} for short) NCs with an icosahedral Au_{12} core protected by two layer gold shells (Au_{42} and Au_{60}).[22] Au_{144} exhibits similar vibration frequencies as those of $[Au_{25}(SR)_{18}]^-$, while the damping was relatively slower.[22,59] After comparing the vibrational coherence results of Au_{144} and Ag_{44} in this work, we found that both of NCs consisted of three layers, which should prevent the vibrational coherence of the innermost core from rapid dephasing. Based on a previous study and results reported here, the robust vibrational coherence observed in the Ag_{44} NCs should be ascribed to their matryoshka-like core–shell structure, which slows the damping of wavepackets by collision with the surrounding environment. The slow dephasing of the vibrational coherence in multi-layer silver NCs should be of importance to their future functions in light harvesting and energy transfer.

Conclusion

In this work, we reported that robust vibrational coherence in the Ag_{44} NCs can be generated *via* ultrafast laser excitation. Significant vibrational coherence with frequencies of 2.4 THz and 1.6 THz can be observed. The coherence in Ag_{44} has a dephasing time of 1 ps at room temperature, which is independent on the excited state relaxation process. Conversely, Ag_{29} shows a relative faster dephasing time, indicating that the robust vibrational coherence in Ag_{44} is ascribed to its unique matryoshka-like core–shell structure, which protects the coherence from dephasing. These results not only provide evidence for the vibrational coherence under ambient conditions but also offer new strategies to prepare long-lived vibrational coherence in metal NCs for use in future applications.

Methods

Sample preparations

The preparation of $[Ag_{44}(SR)_{30}]^{4+}$ (SR = $SPhF_2$) and $Ag_{29}BDT_{12}TPP_4$ (BDT = 1,3-benzenedithiolate) NCs follows the method reported in previous work.[36,60]

Temperature dependent UV-vis-NIR absorption spectra

The steady state absorption spectra were measured using a UV-vis-NIR absorption spectrometer (UV-3600 Plus, Shimadzu). The temperature dependent absorption spectra were obtained using a homemade system comprising the UV-3600Plus absorption spectrometer, a cryostat (OptistatCF2, Oxford Instruments), an electronic temperature controller (MercuryiTC, Oxford Instruments) and a vacuum pump. The temperature was adjusted between 295 K and 78 K, and the sample was dissolved in 2-methyltetrahydrofuran (99%, Alfa Aesar), which can form a clear glass at low temperatures.

Femtosecond and nanosecond transient absorption spectra

Femtosecond TA measurements were performed on a commercial Ti:Sapphire laser (Astrella, Coherent Instruments, Australia, 800 nm, 35 fs, 1.2 mJ, 5 kHz). The pump pulse was generated using a commercial optical parametric amplifier (TOPAS-prime, Light Converison, Lithuania). The probe pulse was produced by focusing a small portion of the 800 nm femtosecond laser into a sapphire plate. The femtosecond pump-probe measurements were performed on a commercial spectrometer (Helios Fire, Ultrafast Systems, USA). The white light and pump beam were overlapped onto the sample, and linear polarizations were set at the magic angle (54.7°) to record the isotropic response. The instrument response function of the whole device was around 100 fs. The pump energy at the sample was about 40 nJ (spot size diameter was about 100 μm). The concentration of samples in different solvents was adjusted to an absorbance of around 0.3 OD at the excitation wavelength in a 1 mm quartz cuvette. No degradation was observed throughout the experiment, and this was confirmed by the steady absorption spectra. The nanosecond TA measurements were conducted using the same pump pulse and an electronically delayed supercontinuum light (EOS, Ultrafast Systems). The low temperature TA measurements were performed in a cryostat (Janis Research), and the sample was dissolved in polystyrene and drop-casted onto the glass to form a uniform thin film.

Quantum chemical calculations

All theoretical calculations were performed using the Gaussian 16 software package. The geometry optimization of the ground state (S_0) of Ag_{44} was calculated using DFT within the D3 dispersion correction at the PBEPBE functional and 6-311G(d,p) basis set (LanL2TZ for Ag).[33,62–67] In addition, the stable geometry of S_0 was verified by vibrational analysis without imaginary frequencies. The single point energy and vertical excitation energy were calculated using time-dependent density functional theory (TDDFT) based on the optimized S_0 geometry.[68–70] To extensively study the excited state properties of Ag_{44}, hole–electron distribution analysis for the $S_0 \rightarrow S_{1/3}$ excitation was further performed using the Multiwfn 3.6 (dev) program.

Data availability

The authors declare that the data supporting the findings of this study are available within the paper and its ESI files.† All relevant data are available from the corresponding author on request.

Author contributions

J. K., W. Z., and Z. K. contributed equally. J. K., Z. K. and W. Z. planned and performed the experiments, analyzed the data, and wrote the manuscript. G. Y. planned and performed the experiments. C. Z., Y. S., H. W. and Y. L assisted with the experimental design and assisted with the data interpretation. M. Z. planned and performed the experiments, acquired funding, analyzed the data, and wrote the manuscript.

Conflicts of interest

The authors declare no conflicts of interest.

Acknowledgements

M. Z. acknowledges the financial support from the Strategic Priority Research Program of the Chinese Academy of Sciences (XDB0450202), National Natural Science Foundation of China (22273095), and Chinese Academy of Sciences (YSBR-007). Y. S. acknowledges the financial support from the Natural Science Foundation of China (22171007). Z. K. acknowledges the financial support from the Natural Science Foundation of China (22303008) and Beijing Natural Science Foundation (2232012).

References

1 G. D. Scholes, G. R. Fleming, L. X. Chen, *et al.*, *Nature*, 2017, **543**, 647–656.
2 J. D. Schultz, J. Y. Shin, M. Chen, J. P. O'Connor, R. M. Young, M. A. Ratner and M. R. Wasielewski, *J. Am. Chem. Soc.*, 2021, **143**, 2049–2058.
3 J. C. Dean and G. D. Scholes, *Acc. Chem. Res.*, 2017, **50**, 2746–2755.
4 S. M. Falke, C. A. Rozzi, D. Brida, M. Maiuri, M. Amato, E. Sommer, A. De Sio, A. Rubio, G. Cerullo, E. Molinari and C. Lienau, *Science*, 2014, **344**, 1001–1005.
5 S. Rafiq and G. D. Scholes, *J. Am. Chem. Soc.*, 2019, **141**, 708–722.
6 G. V. Hartland, *Chem. Rev.*, 2011, **111**, 3858–3887.
7 D. M. Sagar, R. R. Cooney, S. L. Sewall, E. A. Dias, M. M. Barsan, I. S. Butler and P. Kambhampati, *Phys. Rev. B: Condens. Matter Mater. Phys.*, 2008, **77**, 235321.
8 C. Fitzpatrick, J. H. Odhner and R. J. Levis, *J. Phys. Chem. A*, 2020, **124**, 6856–6866.
9 C. J. Bardeen, Q. Wang and C. V. Shank, *Phys. Rev. Lett.*, 1995, **75**, 3410–3413.
10 D. M. Jonas, S. E. Bradforth, S. A. Passino and G. R. Fleming, *J. Phys. Chem.*, 1995, **99**, 2594–2608.
11 S. Rafiq, B. Fu, B. Kudisch and G. D. Scholes, *Nat. Chem.*, 2021, **13**, 70–76.
12 Y. Song, S. N. Clafton, R. D. Pensack, T. W. Kee and G. D. Scholes, *Nat. Commun.*, 2014, **5**, 4933.

13 J. D. Gaynor, J. Sandwisch and M. Khalil, *Nat. Commun.*, 2019, **10**, 5621.
14 S. R. Rather, N. P. Weingartz, S. Kromer, F. N. Castellano and L. X. Chen, *Nature*, 2023, **620**, 776–781.
15 M. Khalil, N. Demirdöven and A. Tokmakoff, *J. Chem. Phys.*, 2004, **121**, 362–373.
16 R. Monni, G. Capano, G. Auböck, H. B. Gray, A. Vlček, I. Tavernelli and M. Chergui, *Proc. Natl. Acad. Sci. U.S.A.*, 2018, **115**, E6396–E6403.
17 M. Pelton, J. E. Sader, J. Burgin, M. Liu, P. Guyot-Sionnest and D. Gosztola, *Nat. Nanotechnol.*, 2009, **4**, 492–495.
18 R. Jin, C. Zeng, M. Zhou and Y. Chen, *Chem. Rev.*, 2016, **116**, 10346–10413.
19 M. Zhou, X. Du, H. Wang and R. Jin, *ACS Nano*, 2021, **15**, 13980–13992.
20 M. Zhou and R. Jin, *Annu. Rev. Phys. Chem.*, 2021, **72**, 121–142.
21 J. Kong, W. Zhang, Y. Wu and M. Zhou, *Aggregate*, 2022, **3**, e207.
22 W. Zhang, J. Kong, Y. Li, Z. Kuang, H. Wang and M. Zhou, *Chem. Sci.*, 2022, **13**, 8124–8130.
23 J. Koivisto, S. Malola, C. Kumara, A. Dass, H. Häkkinen and M. Pettersson, *J. Phys. Chem. Lett.*, 2012, **3**, 3076–3080.
24 P. Maioli, T. Stoll, H. E. Sauceda, I. Valencia, A. Demessence, F. Bertorelle, A. Crut, F. Vallée, I. L. Garzón, G. Cerullo and N. Del Fatti, *Nano Lett.*, 2018, **18**, 6842–6849.
25 M. Y. Sfeir, H. Qian, K. Nobusada and R. Jin, *J. Phys. Chem. C*, 2011, **115**, 6200–6207.
26 M. Zhou, T. Higaki, G. Hu, M. Y. Sfeir, Y. Chen, D.-e. Jiang and R. Jin, *Science*, 2019, **364**, 279–282.
27 H. Qian, M. Y. Sfeir and R. Jin, *J. Phys. Chem. C*, 2010, **114**, 19935–19940.
28 M. Zhou, S. Tian, C. Zeng, M. Y. Sfeir, Z. Wu and R. Jin, *J. Phys. Chem. C*, 2017, **121**, 10686–10693.
29 E. Thyrhaug, S. A. Bogh, M. R. Carro-Temboury, C. S. Madsen, T. Vosch and D. Zigmantas, *Nat. Commun.*, 2017, **8**, 15577.
30 Y.-z. Wu, J. Kong, W. Zhang, S. Wang and M. Zhou, *J. Phys. Chem. C*, 2023, **127**, 13723–13730.
31 W. Zhang, J. Kong, W. Xu, X. Niu, D. Song, W. Liu and A. Xia, *Chin. J. Chem. Phys.*, 2022, **35**, 69–76.
32 X. Yu, W. Pei, W.-w. Xu, Y. Zhao, Y. Su and J. Zhao, *Inorg. Chem.*, 2023, **62**, 20450–20457.
33 Y. Zhong, J. Zhang, T. Li, W. Xu, Q. Yao, M. Lu, X. Bai, Z. Wu, J. Xie and Y. Zhang, *Nat. Commun.*, 2023, **14**, 658.
34 R. Jin, C. Zeng, M. Zhou and Y. Chen, *Chem. Rev.*, 2016, **116**, 10346–10413.
35 Y. Negishi, T. Nakazaki, S. Malola, S. Takano, Y. Niihori, W. Kurashige, S. Yamazoe, T. Tsukuda and H. Häkkinen, *J. Am. Chem. Soc.*, 2015, **137**, 1206–1212.
36 H. Yang, Y. Wang, H. Huang, L. Gell, L. Lehtovaara, S. Malola, H. Häkkinen and N. Zheng, *Nat. Commun.*, 2013, **4**, 2422.
37 M. Zhu, C. M. Aikens, F. J. Hollander, G. C. Schatz and R. Jin, *J. Am. Chem. Soc.*, 2008, **130**, 5883–5885.
38 Y. Wang, X.-H. Liu, Q. Wang, M. Quick, S. A. Kovalenko, Q.-Y. Chen, N. Koch and N. Pinna, *Angew. Chem., Int. Ed.*, 2020, **59**, 7748–7754.
39 M. A. Abbas, P. V. Kamat and J. H. Bang, *ACS Energy Lett.*, 2018, **3**, 840–854.
40 H. Yang, J. Lei, B. Wu, Y. Wang, M. Zhou, A. Xia, L. Zheng and N. Zheng, *Chem. Commun.*, 2013, **49**, 300–302.
41 O. Varnavski, G. Ramakrishna, J. Kim, D. Lee and T. Goodson III, *ACS Nano*, 2010, **4**, 3406–3412.
42 M. Zhou, R. Jin, M. Y. Sfeir, Y. Chen, Y. Song and R. Jin, *Proc. Natl. Acad. Sci. U. S. A.*, 2017, **114**, E4697–E4705.
43 M. S. Devadas, S. Bairu, H. Qian, E. Sinn, R. Jin and G. Ramakrishna, *J. Phys. Chem. Lett.*, 2011, **2**, 2752–2758.
44 Z. Liu, Y. Li, W. Shin and R. Jin, *J. Phys. Chem. Lett.*, 2021, **12**, 1690–1695.
45 J. Mooney, M. M. Krause and P. Kambhampati, *J. Phys. Chem. C*, 2014, **118**, 7730–7739.
46 T. G. Mack, L. Jethi and P. Kambhampati, *J. Phys. Chem. C*, 2017, **121**, 28537–28545.
47 D. P. Strandell and P. Kambhampati, *J. Phys. Chem. C*, 2021, **125**, 27504–27508.
48 Z. Liu, M. Zhou, L. Luo, Y. Wang, E. Kahng and R. Jin, *J. Am. Chem. Soc.*, 2023, **145**, 19969–19981.
49 Y. Wang, Z. Liu, A. Mazumder, C. G. Gianopoulos, K. Kirschbaum, L. A. Peteanu and R. Jin, *J. Am. Chem. Soc.*, 2023, **145**, 26328–26338.
50 O. M. Bakr, V. Amendola, C. M. Aikens, W. Wenseleers, R. Li, L. Dal Negro, G. C. Schatz and F. Stellacci, *Angew. Chem., Int. Ed.*, 2009, **48**, 5921–5926.
51 M. J. Frisch, G. W. Trucks and H. B. Schlegel, *et al.*, *Gaussian, Vol. 16, Revision C.02*, Gaussian, Inc., Wallingford CT, 2019.
52 M. Bursch, J.-M. Mewes, A. Hansen and S. Grimme, *Angew. Chem., Int. Ed.*, 2022, **61**, e202205735.
53 T. Lu and F. Chen, *J. Comput. Chem.*, 2012, **33**, 580–592.
54 M. Pelton, Y. Tang, O. M. Bakr and F. Stellacci, *J. Am. Chem. Soc.*, 2012, **134**, 11856–11859.
55 Y. Yoneda, B. Kudisch, S. Rafiq, M. Maiuri, Y. Nagasawa, G. D. Scholes and H. Miyasaka, *J. Am. Chem. Soc.*, 2021, **143**, 14511–14522.
56 S. Rafiq and G. D. Scholes, *J. Phys. Chem. A*, 2016, **120**, 6792–6799.
57 I. H. M. v. Stokkum, C. C. Jumper, J. J. Snellenburg, G. D. Scholes, R. v. Grondelle and P. Malý, *J. Chem. Phys.*, 2016, **145**, 174201.
58 K. K. Ramankutty, H. Yang, A. Baghdasaryan, J. Teyssier, V. P. Nicu and T. Buergi, *Phys. Chem. Chem. Phys.*, 2022, **24**, 13848–13859.
59 H. Qian, M. Y. Sfeir and R. Jin, *J. Phys. Chem. C*, 2010, **114**, 19935–19940.
60 L. G. AbdulHalim, M. S. Bootharaju, Q. Tang, S. Del Gobbo, R. G. AbdulHalim, M. Eddaoudi, D.-e. Jiang and O. M. Bakr, *J. Am. Chem. Soc.*, 2015, **137**, 11970–11975.
61 W. R. Jeffries, S. Malola, M. A. Tofanelli, C. J. Ackerson, H. Häkkinen and K. L. Knappenberger Jr, *J. Phys. Chem. Lett.*, 2023, **14**, 6679–6685.

62 W.-D. Si, C. Zhang, M. Zhou, W.-D. Tian, Z. Wang, Q. Hu, K.-P. Song, L. Feng, X.-Q. Huang, Z.-Y. Gao, C.-H. Tung and D. Sun, *Sci. Adv.*, 2023, **9**, eadg3587.
63 D. Arima and M. Mitsui, *J. Am. Chem. Soc.*, 2023, **145**, 6994–7004.
64 J. Li, P. Wang and Y. Pei, *J. Phys. Chem. Lett.*, 2022, **13**, 3718–3725.
65 P. Luo, X.-J. Zhai, S. Bai, Y.-B. Si, X.-Y. Dong, Y.-F. Han and S.-Q. Zang, *Angew. Chem., Int. Ed.*, 2023, e202219017.
66 Z.-J. Guan, R.-L. He, S.-F. Yuan, J.-J. Li, F. Hu, C.-Y. Liu and Q.-M. Wang, *Angew. Chem., Int. Ed.*, 2022, **61**, e202116965.
67 X.-L. Pei, Z.-J. Guan, Z.-A. Nan and Q.-M. Wang, *Angew. Chem., Int. Ed.*, 2021, **60**, 14381–14384.
68 D. Lin, M. Zheng and W. W. Xu, *Phys. Chem. Chem. Phys.*, 2020, **22**, 16624–16629.
69 X.-Y. Xie, P. Xiao, X. Cao, W.-H. Fang, G. Cui and M. Dolg, *Angew. Chem., Int. Ed.*, 2018, **57**, 9965–9969.
70 L.-M. Wang, S. Bulusu, H.-J. Zhai, X.-C. Zeng and L.-S. Wang, *Angew. Chem., Int. Ed.*, 2007, **46**, 2915–2918.